Polarization dependence and symmetry analysis in indirect *K*-edge RIXS

G. Chabot-Couture,[1] J. N. Hancock,[2] P. K. Mang,[1] D. M. Casa,[3] T. Gog,[3] and M. Greven[4]
[1]*Department of Applied Physics, Stanford University, Stanford, California 94305, USA*
[2]*Département de Physique de la Matière Condensée, Université de Genève, Genève CH-1211, Switzerland*
[3]*Advanced Photon Source, Argonne National Laboratory, Argonne, Illinois 60439, USA*
[4]*School of Physics and Astronomy, University of Minnesota, Minneapolis, Minnesota 55455, USA*
(Received 28 March 2010; revised manuscript received 28 June 2010; published 15 July 2010)

We present a study of the charge-transfer excitations in undoped Nd_2CuO_4 using resonant inelastic x-ray scattering (RIXS) at the Cu *K*-edge. At the Brillouin zone center, azimuthal scans that rotate the incident-photon polarization within the CuO_2 planes reveal weak fourfold oscillations. A comparison of spectra taken in different Brillouin zones reveals a spectral weight decrease at high-energy loss from forward- to back-scattering. We show that these are scattered-photon polarization effects related to the properties of the observed electronic excitations. Each of the two effects constitutes about 10% of the inelastic signal while the "4*p*-as-spectator" approximation describes the remaining 80%. Raman selection rules can accurately model our data, and we conclude that the observed polarization-dependent RIXS features correspond to E_g and B_{1g} charge-transfer excitations to non-bonding oxygen 2*p* bands, above 2.5 eV energy-loss, and to an E_g $d \rightarrow d$ excitation at 1.65 eV.

DOI: 10.1103/PhysRevB.82.035113 PACS number(s): 74.25.nd, 71.35.−y, 74.72.−h, 78.70.Ck

INTRODUCTION

Raman scattering and optical spectroscopy have enabled tremendous contributions to the study of condensed matter systems. Both probes use ~1 eV light and are limited to essentially zero momentum transfer. In order to investigate the charge response of a material throughout the Brillouin zone, photons in the x-ray regime must be used. X-ray Raman scattering, more commonly referred to as resonant inelastic x-ray scattering (RIXS), allows the measurement of the momentum dependence of charge excitations. Even though it has successfully been used to study the physics of a wide array of systems,[1–5] this resonant technique is relatively new and there is still much to learn about the details of its cross section.

An important strength of conventional Raman scattering is its ability to determine the internal symmetry of excitations by selecting the incident- and scattered-photon polarizations. However, photon polarization effects have only been used to select different electronic excitations when performing RIXS at soft x-ray edges, e.g.: at the O *K* edge or the Cu *L* and *M* edges of the cuprates.[7–11] Equivalent effects have not yet been observed at hard x-ray edges, e.g., the Cu or Mn *K* edges.

For soft x-ray (or "direct"[6]) RIXS, the nature of generated electronic excitations is strongly linked to the incident- and scattered-photon polarizations because the photon absorption and emission processes couple directly with the valence levels. For example, at the Cu *L* edge the incident photon excites a 2*p* core electron directly into the 3*d* valence levels.[34] For hard x-ray (or "indirect"[6]) RIXS, it is unclear whether selecting the incident and scattered photon polarizations can help determine the nature of charge-transfer excitations, because the photon absorption and emission processes are only indirectly coupled to the valence system (through the Coulomb potential of the core hole and of the excited electron). For example, at the Cu *K* edge a 1*s* core electron is excited into the 4*p* band, approximately 10–20 eV above the 3*d* valence levels.

Theoretical models of indirect RIXS typically include only the 1*s* core-hole Coulomb potential and take the 4*p* electron to only be a spectator during the scattering (referred to as the 4*p*-as-spectator approximation),[12–15] because of the large extent of the 4*p* orbital and of its relatively large energy separation from the valence levels. Neglecting the effects of the 4*p* decouples the photon-polarization degrees of freedom from the excitations created in the valence system. So far, investigations of photon polarization effects have concluded that the incident polarization does not affect the valence-band excitations created, but only determines their specific resonance energies (based on the crystal-field levels of the excited 4*p* electron),[14,16,17] as is expected based on the 4*p*-as-spectator approximation. Nonetheless, there still exists no quantitative experimental evidence that the indirect RIXS signal is independent of the incident- and scattered-photon polarizations.

This paper is separated in three parts. In Sec. I, we discuss the photon-polarization dependence expected within the 4*p*-as-spectator approximation. In Sec. II, we study the photon-polarization and scattering-geometry dependence of RIXS at the Cu *K* edge of Nd_2CuO_4 and observe scattered-photon polarization effects beyond the 4*p*-as-spectator approximation. In Sec. II A we present data obtained upon rotating the incident-photon polarization within the CuO_2 planes, while in Sec. II B we present a comparison of zone-center spectra taken in different Brillouin zones. The results are discussed in Sec. III. The normalization procedure used to correct for sample self-absorption and compare RIXS signal across different scattering geometries is described in the Appendix.

I. POLARIZATION DEPENDENCE OF THE RIXS CROSS SECTION

Before presenting our experimental observations of photon polarization effects in RIXS, it is instructive to discuss what is expected according to the current understanding of

the indirect RIXS cross section. At the Cu K edge, the RIXS process starts with the resonant absorption of an x-ray photon which creates a $1s$ core hole and an excited $4p$ electron on the Cu site. During the lifetime of the core hole, before it recombines with the $4p$ electron and an x-ray photon is emitted, the core-hole interacts strongly with the valence system to create electronic excitations. The $4p$ electron, on the other hand, is believed to be only a spectator and to evolve without interacting with the valence system.

In the RIXS process, the initial ($\boldsymbol{\epsilon}_i$) and scattered ($\boldsymbol{\epsilon}_f$) photon polarizations determine the initial and final states of the excited $4p$ electron, and the transition amplitude (I_{4p}) between these two states modulates the RIXS signal, i.e., no RIXS signal is observed if $I_{4p}=0$. Within the $4p$-as-spectator approximation, a simplified model of the evolution of the $4p$ electron during the lifetime of the core-hole ($\hbar/\Gamma$) consists in simplifying its Hamiltonian (H_{4p}) to only two discrete crystal-field levels: $E^{4p}_{x,y}=\Delta$ and $E^{4p}_{z}=0$. Even though it neglects $4p$ band effects, this approach should be valid because, in practice, the RIXS intensity is confined within narrow and well-separated intervals in incident energy. The resulting formula for the transition amplitude describes the photon polarization dependence expected within the $4p$-as-spectator approximation:

$$I_{4p} = \left| \langle 4p(\boldsymbol{\epsilon}_f)| \frac{1}{E_i - H_{4p} - i\Gamma} |4p(\boldsymbol{\epsilon}_i)\rangle \right|^2 = \left| \frac{\epsilon_f^x \epsilon_i^x + \epsilon_f^y \epsilon_i^y}{E_i - \Delta - i\Gamma} + \frac{\epsilon_f^z \epsilon_i^z}{E_i - i\Gamma} \right|^2. \quad (1)$$

In the case where $\Delta \gg \Gamma$, this transition amplitude acts like a polarizer; only the polarization components along the resonating $4p$ crystal-field level contribute to the inelastic signal: $I_{4p} \propto |\epsilon_f^x \epsilon_i^x + \epsilon_f^y \epsilon_i^y|^2$ for an in-plane resonance ($E_i=\Delta$) and $I_{4p} \propto |\epsilon_f^z \epsilon_i^z|^2$ for an out-of-plane resonance ($E_i=0$).

In their study of CuO, Döring *et al.*[18] pointed out that, within the $4p$-as-spectator approximation, the electric dipole absorption-emission matrix element is equivalent to the resonant elastic x-ray scattering cross section described in detail by Hannon *et al.*[19] Furthermore, they successfully apply this approximation to describe the scattering angle dependence of the intensity of the 5.4 eV local charge-transfer excitation in horizontal scattering geometry. Equation (1) is a simplification of the formula presented in Ref. 19 but it succinctly captures the important effect of scattering geometry on the RIXS signal. Including different valence states, such as the well- and poorly-screened intermediate states, would improve it.

In general, Eq. (1) shows that the inelastic intensity is maximized when both the incident- and scattered-photon polarizations are parallel to each other and point along a crystal-field eigenstate. These conditions can naturally be fulfilled in vertical-scattering geometry where both polarizations are perpendicular to the scattering plane (σ polarized).[2,17] For horizontal scattering geometry, with both polarizations within the scattering plane (π polarized), these conditions can only be approached for forward and backward scattering.[20,21]

On the other hand, in horizontal-scattering geometry the elastic intensity can be minimized independently of the inelastic intensity. This can be an advantage since it allows the suppression of the elastic "tail" due to the nonzero energy resolution, leading to a higher signal-to-background ratio. At a scattering angle (2θ) of 90°, the non-resonant elastic contribution is zero because the polarization factor of Thompson scattering ($\boldsymbol{\epsilon}_f \cdot \boldsymbol{\epsilon}_i$) is zero. To have nonzero inelastic intensity, the nondegenerate $4p$ eigenstates can be used as cross-polarizers. By polarizing the incident photon between $4p$ crystal-field eigenstates of different energies, e.g., $\boldsymbol{\epsilon}_i \| \boldsymbol{x}+\boldsymbol{z}$, the inelastic signal will be dominated by the excitations created by the incident photon polarization component along the resonating $4p$ crystal-field eigenstate. Since this resonating component is not perpendicular to the scattered-photon polarization, the resonant inelastic signal will be detectable while the nonresonant elastic signal will be zero. Note that this effectively rotates the photon polarization 90°. This should not be mistaken for a scattered-photon polarization effect where the excited $4p$ electron rotates during the RIXS process.

Scattering at 90° in horizontal geometry has been used extensively.[22,23] Based only on the formula for the $4p$ transition amplitude [Eq. (1)], the maximum RIXS signal in this scattering geometry should be observed when both incident- and scattered-photon polarizations are at 45° from the resonantly excited $4p$ eigenstate. In the tetragonal crystal-field symmetry of cuprates for example, $\boldsymbol{Q} \| \boldsymbol{c}$ and $2\theta=90°$ allows maximum RIXS intensity for both in-plane and out-of-plane resonances while minimizing the nonresonant contribution to the elastic line. As is shown in the Appendix, self-absorption effects will move this maximum of RIXS intensity toward a more grazing incidence angle (keeping $2\theta=90°$) when the scattering surface is perpendicular to the [0 0 L] direction.

II. PHOTON POLARIZATION EFFECTS IN NCO

For our study of the scattering-geometry and photon-polarization dependence of RIXS, we chose Nd_2CuO_4 (NCO), the tetragonal Mott-insulating parent compound of the electron-doped high-temperature superconductor $Nd_{2-x}Ce_xCuO_4$. A single crystal was prepared as described previously[24] and studied in its as-grown state. A larger piece from the same growth was measured with neutron scattering and found to have a Néel temperature $T_N \sim 270$ K.[24]

The RIXS data were collected in vertical scattering geometry with the x-ray spectrometer on beamline 9-ID-B, at the Advanced Photon Source, and using the 2 m arm configuration. The energy resolution (FWHM) was 0.32 eV (Sec. II A) and 0.25 eV (Sec. II B).

The elastic tails due to the elastic peak and nonzero energy resolution are subtracted from the inelastic spectra above 1.5 eV energy loss. This is accomplished by (i) using the elastic peak to establish zero energy transfer, (ii) fitting energy-gain data (typically up to 3 eV) to the heuristic modified Lorentzian form $1/(1+|w|^{\alpha})$ where w is energy-loss (with typical values of α in the range 1–2), (iii) and then subtracting the result of the fit from the energy-loss part of the spectrum.

A. Azimuthal (ψ–) scans

In order to study the effects of photon polarization independently of the momentum transfer, we rotate the incident-photon polarization within the CuO_2 planes while keeping the energy- and momentum-transfer constant by performing azimuthal scans,[25] which are rotations of the sample around an axis parallel to the momentum-transfer (**Q**). In this section, the rotation axis is along the c axis of the sample, as illustrated in Fig. 1(a), for $\omega=0$, and in Fig. 1(b). The azimuthal angle ψ is the scanned variable.

Figure 1(c) presents characteristic RIXS spectra taken at two different incident energies. These line scans show electronic excitations in the 1–10 eV energy-loss range associated with the electronic structure of the strongly-correlated CuO_2 plane, and they indicate the energies where ψ-scans are made. At the incident energy $E_i=8997$ eV, the chosen values span from 1.625 eV, just above the optical charge-transfer gap,[26] to the maximum of the inelastic intensity at 5 eV. At $E_i=9001$ eV, we study the molecular orbital excitation[27] by measuring at 6 eV. The raw azimuthal scans are symmetrized to be consistent with the underlying tetragonal symmetry of the CuO_2 planes. This symmetrization consists in folding back the collected 0–360° ψ-scans within the 0–45° arc, averaging the amplitude of the overlapping data, and statistically combining their error bars. The results are shown in Fig. 1(d). This procedure averages out all non-fourfold components exactly which, in practical terms, filters out experimental noise and leaves only the intrinsic electronic properties. For $E_i=8997$ eV, the resulting amplitudes of the fourfold oscillations are $-0.8\pm3.5\%$ (at 1.625 eV), $-0.2\pm0.9\%$ (2 eV), $3.2\pm0.9\%$ (3.5 eV), and $3.2\pm0.9\%$ (5 eV), while for $E_i=9001$ eV, we find $1.6\pm0.5\%$ (6 eV). Only the last three fourfold oscillations, albeit small, are statistically significant (better than 3σ) and inconsistent with being statistical noise. Fourier analysis of the 'raw' (unsymmetrized) ψ-scan at 3.5 eV ($E_i=8997$ eV) is presented in Fig. 1(f), where the amplitude is in percent of the zerofold (DC) component. Of the four physical components (zero, one, two, fourfold), only the zero, two, and fourfold components are above the statistical noise level.[28] The twofold component is systematically observed in all ψ-scans, but filtered out by the symmetrization procedure.

We can rule out the extrinsic effects of the experimental configuration details as the origin of the observed fourfold oscillations. In the ψ scans, extrinsic effects due to sample self-absorption and to the x-ray beam footprint (the area on the sample illuminated by the incident photon beam) are expected to introduce onefold and twofold oscillations, respectively. In order to minimize these effects, the scattering surface was polished to be normal to the c axis (the ψ-scan rotation axis), and we ensured that the x-ray beam footprint was contained by the sample surface throughout the ψ scans. After this procedure, no measurable onefold component was observed, but a systematic twofold component of 2% remained. This twofold component is observed both within our RIXS signal and with a fluorescence monitor placed below the analyzer. Its strong dependence on the x-ray beam position within the scattering surface confirms that it is a footprint effect. In general, extrinsic effects should be independent of both the selected intermediate state and the final electronic state that is probed and, as a result, be equally prominent for all energy-loss and incident-photon energies. The observed fourfold oscillation amplitude, thus, cannot be due to extrinsic effects because it varies both with incident energy and energy loss. Additionally, the rotation of the anisotropic momentum-resolution ellipsoid in reciprocal space [see Fig. 1(b)], might create an artificial fourfold oscillation

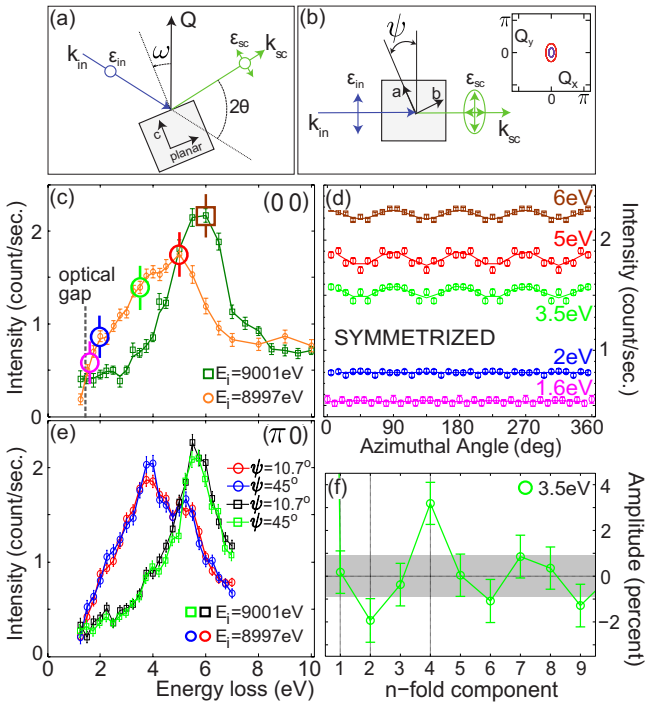

FIG. 1. (Color online) (a) Side and (b) top view of the scattering geometry used throughout this paper. The polarization of the incident beam (σ) and the two possible polarization conditions for the scattered beam (σ and π) are emphasized in both panels. Note that ψ-scans are collected at $\omega=0$ only. (b) Inset: two-dimensional (2D) Brillouin zone: the red line shows the full region of integration arising from the momentum resolution whereas the blue line shows its half width. (c) Energy scans taken at the 2D zone center with incident energy $E_i=8997$ eV (circles) and 9001 eV (squares). The superposed colored circles and square show where the ψ scans of corresponding color and energy are measured in (d) are measured. The charge-transfer gap measured with optical conductivity is indicated for comparison (Ref. 26). (d) Azimuthal scans taken in a full circle around the 2D zone center at 1.625, 2, 3.5, 5 eV energy-loss (for $E_i=8997$ eV) and at 6 eV energy loss for ($E_i=9001$ eV) for $\boldsymbol{Q}=(0\ 0\ 9.1)$ and symmetrized with respect to the 90° rotations and mirror planes of the underlying tetragonal structure. (e) Energy scans with elastic tail subtracted (see text) taken at $\boldsymbol{Q}=(0\ 0.5\ 11.1)$ for different values of the azimuthal angle (ψ). The scans indicated by circles were taken at $E_i=8997$ eV whereas those indicated by squares were taken at $E_i=9001$ eV. Energy scans with $\psi=45°$ are corrected for changes in self-absorption (+5.2%) and incident polarization (+0.8%) compared to $\psi=10.7°$. (f) Fourier components of the raw (unsymmetrized) ψ scan at 3.5 eV energy loss with amplitude given in percent of 0-fold (DC) component (not shown). The fourfold component is well above the statistical noise level (gray region). There is also a twofold component present in the raw data.

pattern in the ψ-scans, but a calculation based on the ellipsoid's shape and on the anisotropy of the momentum-dependent inelastic signal gives an upper bound on this effect to less than 0.05%, much smaller than the observed oscillation amplitudes.

We can also rule out that the fourfold oscillations result from the resonant nature of RIXS, i.e., from the details of the resonantly excited intermediate state. A local distortion of the lattice could in principle introduce a twofold oscillation by splitting the $4p_x$ and $4p_y$ levels of the excited $4p$ electron in the intermediate state, as in the case of the manganites,[25] but because Nd_2CuO_4 has a tetragonal crystal structure, the $4p_x$ and $4p_y$ levels are actually degenerate. On the other hand, a fourfold symmetry is introduced in the intermediate states because the $4p$ states mix non-locally with the valence $3d_{x^2-y^2}$ state. However, two factors make this effect negligible: (i) quadrupole transitions are typically two orders of magnitude weaker than dipole transitions, and (ii) the $3d-4p$ mixing is weak because of small overlap integrals and a large energy separation between the two bands. In general, an intermediate-state effect should be energy-loss independent, i.e., be seen equally in ψ-scans measured at the same incident energy, which is inconsistent with what we observe.

We conclude that the fourfold oscillation is a property of the electronic excitations in the final state. That is, as we vary the energy-loss value, we probe varying admixtures of final states with different symmetries.

Since the incident-photon polarization is kept within the CuO_2 planes during the azimuthal rotations, the $4p$-as-spectator approximation predicts the RIXS signal to be independent of ψ. While this is true of over 90% of the signal (among the ψ-scans presented), the observed fourfold oscillations with peak-to-peak amplitudes up to 6.4% are evidence of excitations created by the interaction of the $4p$ electron with the valence system. Because the $4p$ electron can transfer angular momentum, these excitations can be of a different nature than those created by the $1s$ core-hole. In indirect K-edge RIXS, this result constitutes the first evidence of scattered photon polarization effects beyond the $4p$-as-spectator approximation.

In Fig. 1(e), we extend our analysis beyond the zone center. This figure shows the ψ-angle dependence of the inelastic spectra at $(0\ \ \pi)$ at E_i=8997 eV and 9001 eV. The molecular orbital excitation at 5.6 eV measured for E_i=9001 eV has a weak ψ angle dependence: it is approximately 6% weaker for ψ=45° than for ψ=10.7°. There might also be a ψ-dependent feature for E_i=8997 eV at approximately 3.8 eV.

B. Scattering-geometry dependence

Scattering-geometry dependence of the RIXS signal can have three different origins: sample self-absorption, incident- and scattered-photon polarization effects, and momentum-transfer effects. Since all three generally affect the signal simultaneously, it is difficult to separate their contributions. In Sec. II A, we used a particular scattering geometry that allows for the polarization degrees of freedom to be varied independently of the momentum transfer while minimizing self-absorption effects. Alternatively, the scattering geometry dependence can be investigated by measuring the Brillouin zone dependence of the inelastic signal.

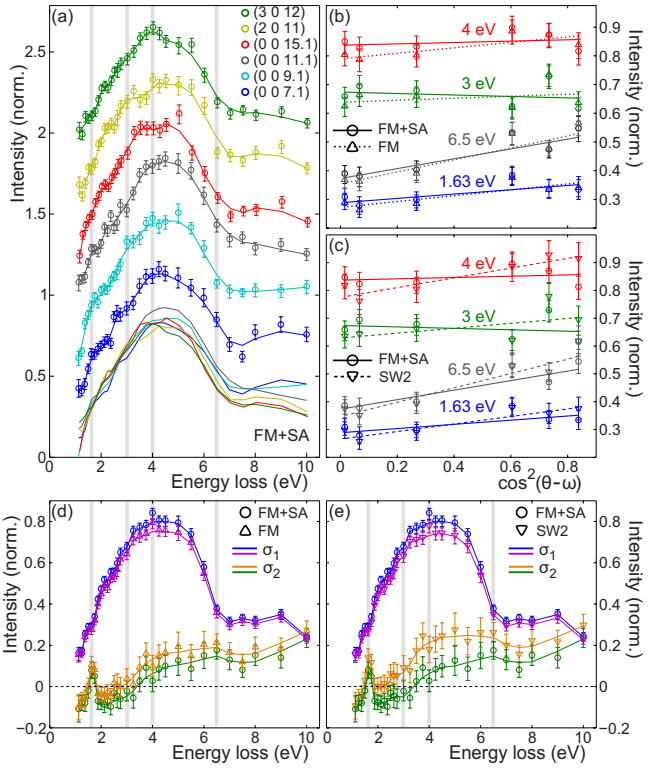

FIG. 2. (Color online) (a) Two-dimensional zone-center spectra collected for a wide range of scattering geometries. Data sets are separated vertically by 0.3 units. The solid lines through the data are smooth interpolations and they are also overlaid at the bottom of the figure to highlight the evolution of the measured spectra. The data sets are scaled using the FM+SA method (see text for details). (b-c) Fits of the Brillouin-zone dependence to the linear form $y=\sigma_1+\sigma_2\cos^2(\theta-\omega)$ at 1.65, 3, 4, and 6.5 eV, comparing the FM+SA normalization procedure with (b) FM and (c) SW2 normalizations. (d-e) Fitted coefficients σ_1 and σ_2 as a function of energy loss, comparing the FM+SA normalization procedure with (d) FM and (e) SW2 normalizations.

Recently, based on remarkable agreement between inelastic spectra taken at high symmetry points of different Brillouin zones, a study of charge-transfer excitations at the Cu K edge of the Mott insulator La_2CuO_4 concluded that the RIXS signal is independent of Brillouin zone.[17] However, a closer look suggests there could be an energy-loss-dependent difference of approximately 10% between spectra measured in different Brillouin zones.

In this Section, in order to study the possibility of a subtle Brillouin-zone dependence, we measure the scattering-geometry dependence of the related Mott insulator Nd_2CuO_4. Inelastic line scans (energy-gain side subtracted) taken at the zone center of six different zones are shown in Fig. 2(a). The proper normalization of each spectrum is important as it allows the comparison of relative intensities even between widely different scattering geometries.

In order to separate extrinsic effects from intrinsic features, we compare four different normalization techniques.

TABLE I. Normalization factors for six different scattering geometries. The raw fluorescence monitor (FM) normalization factors are compared to different correction methods (see text for details).

	Raw	Correction factor			
Q	FM	FM	FM+SA	SW1	SW2
(0 0 7.1)	1.185	1	0.960	1.081	1.091
(0 0 9.1)	0.995	1	0.984	1.065	1.060
(0 0 11.1)	1.000	1	1.000	1.000	1.000
(0 0 15.1)	0.930	1	1.023	1.065	1.003
(2 0 11)	0.966	1	1.043	1.072	0.967
(3 0 12)	0.774	1	1.049	1.077	1.017

The first fluorescence monitor (FM) consists of using the fluorescence signal as a monitor. The second (FM+SA) adds the self-absorption correction described in the Appendix. The third (SW1) and fourth (SW2) both use the fluorescence signal as a monitor and further normalize the spectra by the integrated inelastic spectral weight in a fixed energy-loss range, between 1.4–2.9 eV and 1.9–2.4 eV, respectively. The resulting normalization factors are compiled in Table I where the raw fluorescence monitor factors are separated from the different corrections using either self-absorption or integrated spectral weight. As expected, (0 0 L) scattering geometries (where $\omega=0$) all have approximately the same normalization factor, except for (0 0 7.1), where the x-ray footprint starts to be limited by the scattering surface size. The (H 0 L) grazing-incidence normal-emission geometries (where $\omega<0$) suffer less self-absorption and have lower normalization factors accordingly. Based on the tabulated values, the fluorescence monitor provides the largest contribution to the normalization ($\approx$20%), which validates its use as a first-order self-absorption correction. However, the additional self-absorption correction described in the Appendix is not negligible ($\approx$5%) and should be used.

We analyze the scattering geometry dependence by dividing each of the six energy spectra into energy-loss bins, each bin half the size of the experimental resolution (0.125 eV). Within each bin, the scattering-geometry dependence of the intensity is fitted to a linear form ($y=\sigma_1+\sigma_2 x$), where the dependent variable (x) is either L, $|Q|^2$, or $\cos^2(\theta-\omega)$ [see Fig. 1(a) for the definition of θ and ω]. Each fit is performed using the four different normalization procedures described above.

The quality of each linear fit is characterized by a reduced chi-square $\tilde{\chi}^2$ (the total chi-square divided by the number of degrees of freedom d). The chi-square values and degrees of freedom can be summed across the energy bins to compose a collective reduced chi-square $\tilde{\chi}^2=\Sigma_i\chi_i^2/\Sigma_i d_i$ (i: bin index) which characterizes the fit functions' ability to represent the observed Brillouin-zone dependence across the entire data set. The goodness-of-fit indicator (G) is also calculated.[29]

The values of these two indicators, for each combination of fit function and normalization procedure, are compiled in Table II. The $\cos^2(\theta-\omega)$ linear dependence provides the best fit to our data as it robustly yields the lowest χ^2 and the highest G values, independently of the normalization procedure. The L and $|Q|^2$ fits are poorer, no matter what normalization procedure is used.

TABLE II. Reduced chi-square (χ^2) and goodness-of-fit (G) values for each combination of fit function and normalization procedure.

	$\cos^2(\theta-\omega)$	Q^2	L
	χ^2		
FM	1.433	2.032	2.033
FM+SA	1.513	1.747	1.731
SW1	1.179	1.558	1.543
SW2	1.138	2.062	2.030
	G (%)		
FM	0.13	1.9×10^{-8}	1.8×10^{-8}
FM+SA	0.02	7.7×10^{-5}	1.2×10^{-4}
SW1	8.81	8.8×10^{-3}	1.3×10^{-2}
SW2	14.31	7.2×10^{-9}	2.0×10^{-8}

Examples of the linear $\cos^2(\theta-\omega)$ fits are presented in Figs. 2(b) and 2(c) and compare different normalization procedures. The energy-loss values chosen for this comparison span the spectral range of our data and correspond to the thick and gray vertical lines in Figs. 2(a), 2(d), and 2(e). In Figs. 2(d) and 2(e), the resulting fit parameters (intercept σ_1 and slope σ_2) for each energy bin are compared for three of the four different normalization procedures.

The choice of normalization procedure affects the extracted amount of Brillouin zone dependence. Self-absorption is sensitive to the energy of the scattered photon because its attenuation length changes rapidly near the edge. This attenuation is unimportant for normal emission of the scattered photon (when $\cos^2(\theta-\omega)\approx0$), but it becomes important for grazing emission (when $\cos^2(\theta-\omega)\approx1$). Because of this, using only the FM for normalization overestimates the self-absorption correction for grazing emission, and including the self-absorption correction to the fluorescence monitor normalization (FM+SA) yields a better measure of the Brillouin zone dependence. This is apparent in Figs. 2(b) and 2(d).

Normalizing inelastic spectra collected at different Brillouin zone centers by the spectral weight in a fixed energy-loss range is equivalent to assuming that this spectral weight is independent of Brillouin zone. As a result, the high quality of the SW2 normalization (lowest χ^2 and largest G) suggests that the 1.9–2.4 eV energy-loss range is Brillouin zone independent. On the other hand, this normalization produces unphysically high values of σ_2 (Ref. 30) which suggests that the 1–3 eV energy-loss region in σ_2 is artificially reduced by a source of error beyond the self-absorption correction.

While *a priori* not unphysical,[31] the negative offset in σ_2 below 3 eV (using FM+SA normalization) is probably an artifact of the elastic-line subtraction. In our subtraction of the energy-gain side, we assume that the elastic line is symmetric. While this approximation is in principle valid, weak anisotropic elastic signal could leak into our RIXS spectra (due to the nonzero energy resolution) and introduce an arti-

ficial Brillouin-zone dependence of the signal at low-energy loss. Errors in the fitted elastic line position can also introduce a weak Brillouin zone dependence. While such an anisotropy is limited to low energy loss, an error in fitted position would be proportional to the energy-loss slope of the RIXS spectrum and would create artifacts at both high and low-energy loss. Even though the broad negative offset observed in σ_2 below 3 eV (within FM+SA) could be explained by a Brillouin-zone-varying asymmetry in the elastic line, neither of the above effects can create sharp features such as the one observed at 1.65 eV.

Finally, a slight crystal misalignment could account for the overall larger intensity measured between 3–5 eV at (0 0 11.1), since the zone center spectrum at 8997 eV is a local minimum of inelastic intensity. On the other hand, the difference in spectral shape between (2 0 11) and (3 0 12) around 4 eV is not explicable by a crystal misalignment and could be evidence of a Brillouin-zone dependence not captured by the analysis presented in Fig. 2.

While the many sources of error make the quantitative comparison of the spectra difficult, the quantities σ_1 and σ_2 exhibit robust features. The Brillouin-zone independent part of the RIXS spectrum (σ_1) consists of a broad feature centered at 4.5 eV, a shoulder at 2 eV (and possibly another at 1.4 eV), and a (linearly-extrapolated) onset of 0.8 eV. On the other hand, the Brillouin-zone-dependent part (σ_2) consists of a broad feature, centered around 5 eV with an onset around 2.5 eV, and its most interesting feature is a resolution-limited peak at 1.65 eV.

Because the spectra cannot be scaled to collapse onto one common curve, no matter what normalization is used, the Brillouin-zone dependent part (σ_2) cannot be spurious. The energy-loss dependence also rules out the resonant cross section as the origin of the Brillouin-zone dependence, leaving only the properties of the measured electronic excitations to explain the effect.

For the employed scattering geometry, the $4p$-as-spectator approximation predicts no photon-polarization-based Brillouin-zone dependence of the inelastic signal. Instead, the observed Brillouin-zone dependence is best fit by the $\cos^2(\theta-\omega)$ form which implies that the effect is photon-polarization based and not momentum based. As such, this observation implies that the $4p$ electron interacts with the valence system during the RIXS process.

We note that the integration of the FM+SA normalized σ_2 spectral weight above 2.5 eV[32] sums to $15\pm2\%$ of the integrated σ_1 spectral weight. This departure from the $4p$-as-spectator approximation is larger than the ψ-scan peak-to-peak amplitude variations ($\sim$6%), but it is of the same order of magnitude, which suggests a similar mechanism for both effects.

III. DISCUSSION

The analysis of the incident- and scattered-photon polarization dependence of the cross section is key to probing the symmetry of electronic excitations in Raman scattering.[33] Within (direct) soft RIXS, this has been used to distinguish the Zhang-Rice singlet (ZRS) excitation from local $d\rightarrow d$ excitations.[7,34] On the other hand, for (indirect) hard RIXS, it is unknown what excitation symmetries are measured and what their relative strengths are. It is furthermore unknown if RIXS obeys selection rules linking the incident- and scattered-photon polarizations and the underlying excitation symmetries.

While theoretical treatments have made assumptions about what types of excitations are measurable, they have not discussed selection rules explicitly. Treatments using joint-density-of-states-type cross sections limit the scattering from the core-hole to interband transitions between bands of the same point-group symmetry at $\boldsymbol{Q}=0$.[35,36] Furthermore, calculated RIXS spectra using one-band Hubbard models are automatically limited to states of x^2-y^2 local symmetry (the ZRS combination of oxygen orbitals is an x^2-y^2 combination of the O p_σ orbitals), so that the symmetry of the charge-transfer excitations is limited to A_{1g} at $\boldsymbol{Q}=0$.[37] On the other hand, non-A_{1g} transitions have been suggested to explain new features in measured RIXS spectra: charge-transfers to nonbonding bands[4] and local $d\rightarrow d$ excitations[38] are both examples of such non-A_{1g} transitions.

While it remains unclear if the polarization-based Raman selection rules can be applied to interpret the photon-polarization dependence of indirect RIXS spectra at the Brillouin zone center (zero reduced $\boldsymbol{q}$), we test their applicability by comparing their predictions to our data. From the definition of the symmetry channels allowed by the tetragonal (D_{4h}) crystal structure of Nd_2CuO_4 (A_{1g}, A_{2g}, B_{1g}, B_{2g}, and E_g) and the evolution of the incident- and scattered-photon polarizations with the azimuthal angle (ψ) and the angular difference ($\theta-\omega$), we can write the photon-polarization-based Raman selection rules, at $\boldsymbol{Q}=0$,[33] as a function of the scattering power within each allowed symmetry channel:

$$\begin{aligned} I_{\text{Inel.}} \propto & [\sigma(A_{1g})+\sigma(A_{2g})+\sigma(B_{1g})+\sigma(B_{2g})] \\ & +[\sigma(E_g)-\sigma(B_{1g})-\sigma(A_{2g})]\cos^2(\theta-\omega) \\ & +[\sigma(B_{1g})-\sigma(B_{2g})]\cos^2(2\psi)\cos^2(\theta-\omega). \end{aligned} \quad (2)$$

Since the scattered-photon polarization is not analyzed, we must include both the σ and π channels (polarization perpendicular and parallel to the scattering plane, respectively), as shown in Figs. 1(a) and 1(b). Note that these rules inform us about the polarization dependence of these symmetry channels, but not about their relative size.

At fixed θ and for $\omega=0$, Eq. (2) can be rewritten as $\sigma_0+\sigma_4\cos^2(2\psi)$, which is precisely the functional form of the fourfold oscillations presented in Sec. II A. With a peak-to-peak fourfold amplitude equal to $[\sigma(B_{1g})-\sigma(B_{2g})]\cos^2(\theta-\omega)$, these azimuthal oscillations can be interpreted in terms of the B_{1g} and B_{2g} symmetry channels. While we cannot determine the B_{1g} and B_{2g} amplitudes independently, our data suggest the presence of B_{1g}-type electronic excitations at 3.5 and 5 eV energy loss for $E_i=8997$ eV and at 6 eV for $E_i=9001$ eV. Correcting the fourfold peak-to-peak amplitude to account for the $\cos^2(\theta-\omega)$ dependence ($\theta=31°$ and $\omega=0°$), we obtain an adjusted $B_{1g}-B_{2g}$ amplitude of +8.7% (σ_4/σ_0) between

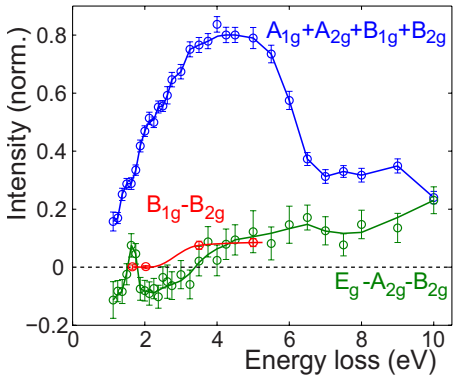

FIG. 3. (Color online) Symmetry interpretation of the photon-polarization dependent and independent RIXS spectral weight for tetragonal Nd_2CuO_4. While composed of many different symmetry channels, the blue spectrum is most likely dominated by the A_{1g} symmetry channel. See text for details.

3.5–5 eV for E_i=8997 eV. These adjusted data are shown in Fig. 3.

For ψ=0, Eq. (2) reduces to a cross section of the form $\sigma_1+\sigma_2\cos^2(\theta-\omega)$, where $\sigma_1=A_{1g}+A_{2g}+B_{1g}+B_{2g}$ and $\sigma_2=E_g-A_{2g}-B_{2g}$, which is precisely the function that best fits the Brillouin-zone dependence presented in Sec. II B. This suggests that the decrease in spectral weight toward backscattering observed here for Nd_2CuO_4 can be interpreted in terms of E_g excitations at high-energy loss. These symmetry assignments for σ_1 and σ_2 are reproduced in Fig. 3.

In tetragonal symmetry, the incident- and scattered-photon polarizations of an E_g excitation correspond to $4p$ crystal-field eigenstates with different energies (e.g., $x\rightarrow z$ or $z\rightarrow x$), unlike the A_{1g}, A_{2g}, B_{1g}, and B_{2g} symmetry channels where the initial and final $4p$ crystal-field eigenstates are degenerate (and planar). This creates a unique resonance profile[17,18,23,39] for E_g excitations, which can increase or decrease their intensity compared to the other symmetry channels.

For example, in the scattering geometry used here, at the incident energy E_i=8997 eV, E_g and B_{1g} excitations have the same incident-photon polarization resonance but their scattered-photon polarization resonances differ. For B_{1g} excitations, the scattered-photon polarization is $\epsilon_f=x$ and the final energy resonance is at E_f=8997 eV whereas for E_g excitations, the scattered-photon polarization is $\epsilon_f=z$ and there are scattered-photon resonances at E_f=8985, 8993, and 8997 eV according to the XAS data in Fig. 4. Around 4 and 12 eV energy loss, the scattered photon coincides with an out-of-plane resonance and E_g excitations are enhanced compared to B_{1g} excitations. In this case, assuming that both symmetry channels have a comparable density of states, we estimate that E_g excitations are enhanced by a factor of 2–5. If we correct for this enhancement, the observed 15% Brillouin-zone dependence becomes a 3%–8% effect, more comparable to the 8.7% azimuthal-angle dependence [6.4%, corrected for the $\cos^2(\theta-\omega)$ factor].

For the scattering geometry used here, the core-hole potential is expected to create the majority of the inelastic signal because it has the strongest effect on the valence system. We suggest that the Brillouin-zone-independent and ψ-angle-independent spectral weight is created by core-hole scattering and consists of A_{1g} symmetry. We note, however, that this contribution can be reduced to zero in certain scattering geometries because its cross section should follow the $4p$-as-spectator transition amplitude discussed in Sec. I.

While we have shown that the Raman selection rules can accurately model the observed photon-polarization effects and suggest symmetry assignments for different inelastic features, these assignments should be supported by a theoretical understanding of the excitations. The molecular orbital (MO) excitation at the poorly screened state is understood to be of A_{1g} symmetry, which is consistent with its weak ψ-angle dependence at (0 π) [see Fig. 1(e)]. While the MO excitation does show a weak fourfold oscillation at the zone center, a comparison of the (0 π) and (0 0) spectra suggests that the fourfold oscillation might instead be a property of a momentum-dependent shoulder that disappears away from (0 0).

In principle, $d\rightarrow d$ excitations provide a testing ground for the validity of Raman selection rules within RIXS, and such excitations have been well studied with soft x-ray RIXS at the Cu $L-$ (Refs. 8–10, 40, and 41) and M-edges,[11] with optical absorption,[42] with large-shift Raman scattering,[43] and with different theoretical methods.[44,45]

Although for Nd_2CuO_4 only the $A_{2g}(d_{x^2-y^2}\rightarrow d_{xy})$ Cu crystal-field excitation has been observed around 1.4 eV,[43] the crystal-field excitations of tetragonal $Sr_2CuO_2Cl_2$ have been extensively studied[10,11,42,44] and their energies should be similar to those of Nd_2CuO_4. For the latter, Raman selection rules suggest that the resolution-limited feature we observe at 1.65 eV (Fig. 2) is of E_g symmetry. The E_g crystal-field excitation $(d_{x^2-y^2}\rightarrow d_{xz})$ in $Sr_2CuO_2Cl_2$ has an energy of 1.7 eV which, supports this symmetry assignment and the applicability of the Raman selection rules.

A complete determination of the $d\rightarrow d$ excitations in tetragonal Nd_2CuO_4 should be possible with the experimental methods described in this paper, i.e., without analyzing the scattered-photon polarization, since only three types of $d\rightarrow d$ excitations are possible (the B_{2g} symmetry change does not exist within the Cu $3d$ orbitals). For example, with better energy resolution, the A_{2g} excitation should be observable at 1.4 eV with a Brillouin-zone dependence study, whereas the $B_{1g}(d_{x^2-y^2}\rightarrow d_{3z^2-r^2})$ excitation should be observable with a ψ-angle dependence study.

Charge-transfers from the nonbonding oxygen bands to the upper Hubbard band, which have been used to explain the multiplet of inelastic features between 2 and 6 eV,[4] are expected to be of non-A_{1g} symmetry. As studied with ARPES,[46–48] O $2p$ non-bonding bands have approximately 1.5 eV more binding energy than the ZRS band. Accordingly, the RIXS charge transfer to such bands should start at an energy 1.5 eV above the overall onset of RIXS excitations. In Nd_2CuO_4, the onset of excitations is approximately 0.8 eV, while the fourfold azimuthal-scan oscillations start between 2 and 3.5 eV and the broad feature in the Brillouin-zone-dependent part starts at around 2.5 eV, i.e., both photon-polarization-dependent features have onsets approximately 1.5 eV above 0.8 eV. As a result, they could be charge-transfers excitations to oxygen nonbonding bands.

In their EELS study of $Sr_2CuO_2Cl_2$, Moskvin *et al.*[49] identify many charge-transfer excitations, three of which have A_{1g} symmetry and should be RIXS active. The two strongest excitations are around 8 eV, but do not have obvious RIXS equivalents. Finally, the third A_{1g} excitation at 2 eV, just above the optical gap, is identified as the Zhang-Rice singlet. This may correspond to the 2 eV feature in RIXS, which is apparent as a weak shoulder in Figs. 2(d) and 2(e) and is seen as a clear peak in La_2CuO_4 and $Sr_2CuO_2Cl_2$. This suggests that the 2 eV feature in RIXS is of A_{1g} symmetry. An exact diagonalization calculation[50] of charge-transfer excitations within a one-band Hubbard model of the CuO_2 plane agree quite well with our data and the A_{1g} symmetry assignment of the 2 eV feature. The calculation shows a peak at 2 eV that is exclusively of A_{1g} symmetry, and a continuum of excitations between 2–3.5 eV that is of predominantly A_{1g} character, in good agreement with the symmetry interpretation of our data. The relative intensity of these two features disagrees with our observations, but quantitative agreement is not expected, since the resonant and non-resonant cross sections are very different.

In order to better understand the symmetry selectivity of the RIXS cross section, it is worthwhile to compare it to well-established probes. On the other hand, symmetry-selectivity differs from probe to probe, which renders direct comparisons hazardous. For example, in crystals with an inversion center, optical conductivity measures a current-current correlation function only sensitive to *ungerade* excitations, while electron-energy-loss-spectroscopy (EELS) and IXS measure a density-density correlation function that is sensitive to both *ungerade* and *gerade* excitations. Furthermore, the symmetry-sensitivity of these probes has a strong and non-periodic $\boldsymbol{Q}$-dependence[51,52] in contrast to the nearly Brillouin-zone independent RIXS spectra.

CONCLUSION

By studying the photon-polarization dependence of indirect RIXS at the Cu K-edge of the tetragonal Mott insulator Nd_2CuO_4, we uncover anomalous excitations of two different types, which is evidence of scattered-photon polarization effects. While the majority (80%) of the inelastic signal is describable by the $4p$-as-spectator approximation, the anomalous remainder constitutes the first evidence of RIXS excitations created by the interaction of the excited $4p$ electron with the valence system.

The successful modeling of the observed azimuthal-scan fourfold patterns and of the Brillouin-zone dependence by photon-polarization-based Raman selection rules suggests that these rules can be used to interpret zone-center RIXS spectra. Using these rules, we tentatively assign the sharp peak at 1.65 eV in the Brillouin-zone-dependent spectral weight to an E_g $d \rightarrow d$ excitation and the broad features above 2.5 eV in both the Brillouin-zone-dependent and azimuthal-angle-dependent spectral weight to E_g and B_{1g} charge-transfers to nonbonding oxygen bands.

Establishing photon-polarization-based methods to characterize the electronic excitations' symmetry is a pivotal challenge for RIXS. Such methods should facilitate the interpretation of experimental spectra and help provide a better understanding of the underlying physics of the cuprates and other transition metal oxides. While a complete scattered-photon polarization analysis is currently prohibited by low count rates, ongoing instrumentation development and future increases in photon flux should soon make the full polarization analysis of the inelastic signal possible.

ACKNOWLEDGMENTS

We would like to acknowledge valuable conversations with J. van den Brink, T. P. Devereaux, and K. Ishii. This work was supported by the DOE under Contract No. DE-AC02-76SF00515 and by the NSF under Grant No. DMR-0705086.

APPENDIX: RIXS NORMALIZATION WITH A FLUORESCENCE MONITOR

Aside from effects intrinsic to the cross section, the RIXS scattering intensity is also modulated by the sample self-absorption, an extrinsic effect that depends on the scattering geometry. In x-ray scattering, the absorption processes which determine the x-ray absorption length of a crystal are dominated by Auger emission of electrons and core-level fluorescence lines. Together, the cross sections of these processes dwarf the RIXS cross section. As a result, when the x-ray beam travels through the sample, before and after the RIXS event, its intensity is attenuated. This attenuation has a strong dependence on the scattering geometry and determines the illuminated sample volume. The RIXS signal is proportional to the number of Cu atoms resonantly excited in this volume. This attenuation is referred to as self-absorption, and correcting for it is common practice for other spectroscopic scattering probes (for example, in EELS,[53] in EXAFS,[54] and in direct RIXS[55]) but has not yet become standard for indirect RIXS.

To calculate this effect, we must know the x-ray absorption length and the scattering geometry. In reflection geometry, the RIXS intensity given by Eq. (A1). It includes the incident beam intensity I_0, the intrinsic RIXS scattering amplitude per Cu atom $F(E_i, \Delta E)$, the incident beam cross-sectional area B_a, the density of Cu atoms ρ_{Cu}, the absorption coefficient for the incident (scattered) photons $\mu_i(\mu_f)$ with polarization $\boldsymbol{\epsilon}_i(\boldsymbol{\epsilon}_f)$ and energy E_i (E_f), as well as the scattering angles θ_i and θ_f given relative to the sample surface, as shown in Fig. 4(b). The maximum scattering intensity is obtained for a photon with grazing incidence which is emitted perpendicular to the sample surface [an example is shown in Fig. 4(b)]. In turn, the minimum intensity is observed for normal incidence and grazing emission angle. The reduction in RIXS signal from having a footprint (the beam spot on the sample) larger than the scattering surface is not included but is an important effect at grazing incidence.

$$I = (I_0 \rho_{Cu} B_a) S(E_i, \boldsymbol{\epsilon}_i, E_f, \boldsymbol{\epsilon}_f) F(E_i, E_i - E_f)$$
$$= \frac{I_0 \rho_{Cu} B_a}{\mu(\boldsymbol{\epsilon}_i, E_i) + \mu(\boldsymbol{\epsilon}_f, E_f) \dfrac{\sin(\theta_i)}{\sin(\theta_f)}} F(E_i, E_i - E_f). \quad \text{(A1)}$$

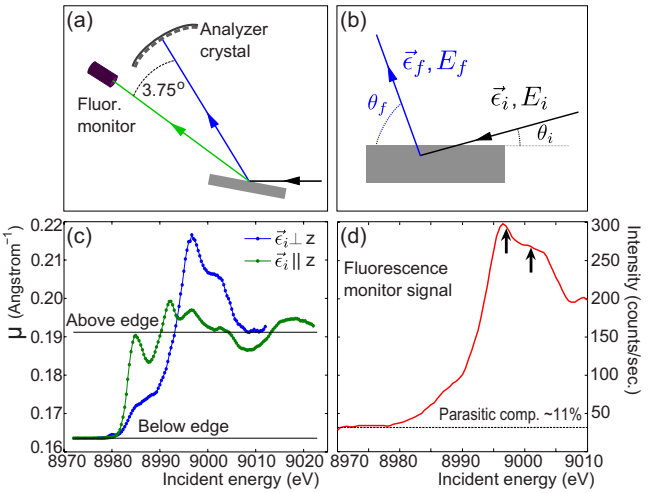

FIG. 4. (Color online) (a) Position of the fluorescence monitor relative to the analyzer crystal (b) Self-absorption parameters in reflection geometry. (c) X-ray absorption spectroscopy (XAS) data (by partial fluorescence yield of the Cu $K_{\alpha 1}$ emission line) in the Cu K-edge region. The black lines correspond to the calculated x-ray absorption coefficients above and below the Cu K edge for Nd_2CuO_4. The measured XAS curves are scaled to follow the published curves by Tranquada *et al.* (Ref. 56). (d) Nd_2CuO_4 absorption curve at the Cu K edge measured with the fluorescence monitor as described in the text. The black arrows indicate incident energies of 8997 and 9001 eV.

In an ideal experiment, this formula could be used directly to normalize the RIXS spectra taken in different scattering geometries. In practice though, the footprint is highly dependent on the scattering surface and can affect the RIXS signal in nontrivial ways. To counteract this difficulty, we use a fluorescence detector put at a known position close to the analyzer crystal, as presented in Fig. 4(a). After measuring the position of the sample surface relative to the crystal axes and tuning the fluorescence detector to an emission line (for example Cu $K_{\alpha 1}$), we can calculate the scattering geometry dependence of both the FM signal (S_{FM}) and of the RIXS signal (S_{RIXS}). In order to correct for the self-absorption effect, we normalize with the following ratio:

$$I^C_{RIXS} = \frac{I_{RIXS}}{I_{FM}} \times \frac{S_{FM}}{S_{RIXS}}, \tag{A2}$$

where the measured RIXS and fluorescence intensities are I_{RIXS} and I_{FM}, respectively. Simply dividing the RIXS signal by the FM signal is a first-order correction that can partially account for changes in the x-ray footprint on the sample. However, the exact correction must include variations in x-ray self-absorption based on the scattering geometry, the photon's polarization and energy, all of which require calculating the self-absorption factors S_{FM} and S_{RIXS}. Note that the S_{FM} calculation includes the difference in location between the spectrometer's analyzer crystal and the fluorescence monitor, as shown in Fig. 4(a). In practice, the further away the FM is placed from the analyzer crystal, the more difficult it will be to accurately account for positional differences in the calculation of the self-absorption correction. This can become a large source of systematic error in the normalization procedure, although this is not the case in the present experiment.

In the experiments presented above, the fluorescence signal was collected with a solid-state detector (Amptek). The signal was then fed into a scaler and only photons within a fixed energy range were counted, in our case, in a 1 keV range around the strong Cu $K_{\alpha 1}$ emission line at 8.1 keV. An absorption curve for Nd_2CuO_4 with in-plane incident-photon polarization collected with this fluorescence monitor is presented in Fig. 4(d). The nonzero signal below the absorption edge is parasitic but is not the result of dark current within the detector. Instead, it is composed of two signals that leak into the energy integration window: elastic scattering at 9 keV and neodymium L-edge fluorescence at 7 keV. Within our theoretical calculation, this parasitic component is tentatively compensated for by modeling it as 70% elastic signal and 30% neodymium fluorescence. Since the parasitic component does not vary congruently with the measured emission line, it constitutes a source of error and should in general be minimized.

In order to calculate the polarization dependent x-ray absorption coefficients (μ) in the Cu K-edge region, we collected x-ray absorption data by partial fluorescence yield at the Cu $K_{\alpha 1}$ emission line with an x-ray spectrometer.[57] The effect of self-absorption, typically important close to absorption edges, was calculated as described by Carboni *et al.*,[58] but was not significant here. In order to complete the construction of the absorption coefficients, the curves were then scaled to match the tabulated values for x-ray absorption in Nd_2CuO_4 above and below the Cu K edge and following Ref. 56. The results are shown in Fig. 4(c). While both the normalization procedure above the edge and the self-absorption correction of the fluorescence signal are sources of error, a conservative estimation of their effects is included in the normalization factor's error although they are negligible here.

This correction procedure includes absorption effects due to changes of the scattered-photon energy that simply normalizing to the fluorescence signal cannot account for. For example, based on Fig. 4(c), an incident in-plane photon with an energy of 8997 eV would see more absorption when entering the sample than a 10 eV energy-loss (E_f=8987 eV) scattered photon leaving the sample. As such, the high energy-loss part of a RIXS spectrum collected at E_i=8997 eV (and only normalized to the fluorescence signal) would be artificially too high.

Finally, the scattered photon can in principle have σ or π polarization, which affects the calculated self-absorption correction. In vertical scattering geometry, at the in-plane $4p$ resonance, and within the bounds of the $4p$-as-spectator approximation, the scattered photon must be σ polarized and we calculate the self-absorption correction based on this prescription. As seen in Sec. II B, there is evidence that this approximation only describes part of the RIXS signal, with part of the complementary contribution in the π polarization channel. This latter polarization channel, when isolated, can be normalized by modifying the calculated scattered photon x-ray absorption coefficient (μ_f) accordingly and multiplying the $\sigma \rightarrow \pi$ scattering intensity by the ratio of the $\sigma \rightarrow \pi$ and

$\sigma \rightarrow \sigma$ calculated self-absorption corrections:

$$f_{RIXS}^{\sigma \rightarrow \pi} = \frac{S^{\sigma \rightarrow \pi}}{S^{\sigma \rightarrow \sigma}}. \quad \text{(A3)}$$

On the other hand, within the measured spectral range, the maximum correction is only 4% of the Brillouin-zone-dependent signal and does not noticeably affect the normalization outlined above.

[1] S. Grenier, J. P. Hill, V. Kiryukhin, W. Ku, Y.-J. Kim, K. J. Thomas, S.-W. Cheong, Y. Tokura, Y. Tomioka, D. Casa, and T. Gog, Phys. Rev. Lett. **94**, 047203 (2005).

[2] J. P. Hill, G. Blumberg, Y.-J. Kim, D. S. Ellis, S. Wakimoto, R. J. Birgeneau, S. Komiya, Y. Ando, B. Liang, R. L. Greene, D. Casa, and T. Gog, Phys. Rev. Lett. **100**, 097001 (2008).

[3] S. Huotari, T. Pylkkänen, G. Vankó, R. Verbeni, P. Glatzel, and G. Monaco, Phys. Rev. B **78**, 041102 (2008).

[4] L. Lu, G. Chabot-Couture, X. Zhao, J. N. Hancock, N. Kaneko, O. P. Vajk, G. Yu, S. Grenier, Y. J. Kim, D. Casa, T. Gog, and M. Greven, Phys. Rev. Lett. **95**, 217003 (2005).

[5] J. N. Hancock, G. Chabot-Couture, Y. Li, G. A. Petrakovskiĭ, K. Ishii, I. Jarrige, J. Mizuki, T. P. Devereaux, and M. Greven, Phys. Rev. B **80**, 092509 (2009).

[6] J. van den Brink and M. van Veenendaal, EPL **73**, 121 (2006).

[7] K. Okada and A. Kotani, Phys. Rev. B **65**, 144530 (2002).

[8] Y. Harada, K. Okada, R. Eguchi, A. Kotani, H. Takagi, T. Takeuchi, and S. Shin, Phys. Rev. B **66**, 165104 (2002).

[9] L. C. Duda, G. Dräger, S. Tanaka, A. Kotani, J. Guo, D. Heumann, S. Bocharov, N. Wassdahl, and J. Nordgren, J. Phys. Soc. Jpn. **67**, 416 (1998).

[10] G. Ghiringhelli, N. B. Brookes, E. Annese, H. Berger, C. Dallera, M. Grioni, L. Perfetti, A. Tagliaferri, and L. Braicovich, Phys. Rev. Lett. **92**, 117406 (2004).

[11] P. Kuiper, J.-H. Guo, C. Såthe, L.-C. Duda, J. Nordgren, J. J. M. Pothuizen, F. M. F. de Groot, and G. A. Sawatzky, Phys. Rev. Lett. **80**, 5204 (1998).

[12] K. Tsutsui, T. Tohyama, and S. Maekawa, Phys. Rev. Lett. **83**, 3705 (1999).

[13] J. I. Igarashi, T. Nomura, and M. Takahashi, Phys. Rev. B **74**, 245122 (2006).

[14] F. Vernay, B. Moritz, I. S. Elfimov, J. Geck, D. Hawthorn, T. P. Devereaux, and G. A. Sawatzky, Phys. Rev. B **77**, 104519 (2008).

[15] L. J. P. Ament, F. Forte, and J. van den Brink, Phys. Rev. B **75**, 115118 (2007).

[16] K. Hämäläinen, J. P. Hill, S. Huotari, C.-C. Kao, L. E. Berman, A. Kotani, T. Idé, J. L. Peng, and R. L. Greene, Phys. Rev. B **61**, 1836 (2000).

[17] Y.-J. Kim, J. P. Hill, S. Wakimoto, R. J. Birgeneau, F. C. Chou, N. Motoyama, K. M. Kojima, S. Uchida, D. Casa, and T. Gog, Phys. Rev. B **76**, 155116 (2007).

[18] G. Döring, C. Sternemann, A. Kaprolat, A. Mattila, K. Hämäläinen, and W. Schülke, Phys. Rev. B **70**, 085115 (2004).

[19] J. P. Hannon, G. T. Trammell, M. Blume, and D. Gibbs, Phys. Rev. Lett. **61**, 1245 (1988).

[20] E. Collart, A. Shukla, J.-P. Rueff, P. Leininger, H. Ishii, I. Jarrige, Y. Q. Cai, S.-W. Cheong, and G. Dhalenne, Phys. Rev. Lett. **96**, 157004 (2006).

[21] M. Z. Hasan, P. A. Montano, E. D. Isaacs, Z.-X. Shen, H. Eisaki, S. K. Sinha, Z. Islam, N. Motoyama, and S. Uchida, Phys. Rev. Lett. **88**, 177403 (2002).

[22] K. Ishii, K. Tsutsui, Y. Endoh, T. Tohyama, S. Maekawa, M. Hoesch, K. Kuzushita, M. Tsubota, T. Inami, J. Mizuki, Y. Murakami, and K. Yamada, Phys. Rev. Lett. **94**, 207003 (2005).

[23] L. Lu, J. N. Hancock, G. Chabot-Couture, K. Ishii, O. P. Vajk, G. Yu, J. Mizuki, D. Casa, T. Gog, and M. Greven, Phys. Rev. B **74**, 224509 (2006).

[24] P. K. Mang, O. P. Vajk, A. Arvanitaki, J. W. Lynn, and M. Greven, Phys. Rev. Lett. **93**, 027002 (2004).

[25] Y. Murakami, J. P. Hill, D. Gibbs, M. Blume, I. Koyama, M. Tanaka, H. Kawata, T. Arima, Y. Tokura, K. Hirota, and Y. Endoh, Phys. Rev. Lett. **81**, 582 (1998).

[26] Y. Onose, Y. Taguchi, K. Ishizaka, and Y. Tokura, Phys. Rev. B **69**, 024504 (2004).

[27] Y.-J. Kim, J. P. Hill, G. D. Gu, F. C. Chou, S. Wakimoto, R. J. Birgeneau, S. Komiya, Y. Ando, N. Motoyama, K. M. Kojima, S. Uchida, D. Casa, and T. Gog, Phys. Rev. B **70**, 205128 (2004).

[28] While the unphysical ninefold component is above noise level, its amplitude is 1.4σ and is not statistically inconsistent with being zero.

[29] The goodness-of-fit indicator (G) is another metric to quantify the quality of a fit. It depends on the number of degrees of freedom and the χ^2 such that, given a chi-square distribution, G is the probability that a randomly obtained χ^2 value be bigger than the one resulting from the fit. Typically, a fit with G above 10% is judged good. However, this value is not hard set and the distribution of errors or their systematics should be taken into account and can make smaller values of G acceptable.

[30] The ratio of the integrated spectral weight in the σ_2 and σ_1 channels for SW2 normalization is 39% compared to 15% for FM+SA.

[31] They correspond to an increase in the RIXS spectral weight towards backscattering.

[32] We do not include the negative region at low-energy loss since it is most likely a systematical error introduced by the elastic line subtraction.

[33] T. P. Devereaux and R. Hackl, Rev. Mod. Phys. **79**, 175 (2007).

[34] M. van Veenendaal, Phys. Rev. Lett. **96**, 117404 (2006).

[35] M. Takahashi, J.-I. Igarashi, and T. Semba, J. Phys.: Condens. Matter **21**, 064236 (2009).

[36] R. S. Markiewicz and A. Bansil, Phys. Rev. Lett. **96**, 107005 (2006).

[37] T. Tohyama, K. Tsutsui, and S. Maekawa, J. Phys. Chem. Solids **66**, 2139 (2005).

[38] D. S. Ellis, J. P. Hill, S. Wakimoto, R. J. Birgeneau, D. Casa,

T. Gog, and Y.-J. Kim, Phys. Rev. B **77**, 060501 (2008).
[39] P. Abbamonte, C. A. Burns, E. D. Isaacs, P. M. Platzman, L. L. Miller, S. W. Cheong, and M. V. Klein, Phys. Rev. Lett. **83**, 860 (1999).
[40] G. Ghiringhelli *et al.*, Eur. Phys. J. Spec. Top. **169**, 199 (2009).
[41] L.-C. Duda, J. Nordgren, G. Dräger, S. Bocharov, and T. Kirchner, J. Electron Spectrosc. Relat. Phenom. **110-111**, 275 (2000).
[42] J. D. Perkins, J. M. Graybeal, M. A. Kastner, R. J. Birgeneau, J. P. Falck, and M. Greven, Phys. Rev. Lett. **71**, 1621 (1993).
[43] D. Salamon, R. Liu, M. V. Klein, M. A. Karlow, S. L. Cooper, S. W. Cheong, W. C. Lee, and D. M. Ginsberg, Phys. Rev. B **51**, 6617 (1995).
[44] D. S. Middlemiss and W. C. Mackrodt, J. Phys.: Condens. Matter **20**, 015207 (2008).
[45] C. de Graaf and R. Broer, Phys. Rev. B **62**, 702 (2000).
[46] J. J. M. Pothuizen, R. Eder, N. T. Hien, M. Matoba, A. A. Menovsky, and G. A. Sawatzky, Phys. Rev. Lett. **78**, 717 (1997).
[47] R. Hayn, H. Rosner, V. Y. Yushankhai, S. Haffner, C. Dürr, M. Knupfer, G. Krabbes, M. S. Golden, J. Fink, H. Eschrig, D. J. Singh, N. T. Hien, A. A. Menovsky, C. Jung, and G. Reichardt, Phys. Rev. B **60**, 645 (1999).
[48] A. Damascelli, Z. Hussain, and Z.-X. Shen, Rev. Mod. Phys. **75**, 473 (2003).
[49] A. S. Moskvin, R. Neudert, M. Knupfer, J. Fink, and R. Hayn, Phys. Rev. B **65**, 180512 (2002).
[50] T. Tohyama, J. Phys. Soc. Jpn. **75**, 034713 (2006).
[51] M. W. Haverkort, A. Tanaka, L. H. Tjeng, and G. A. Sawatzky, Phys. Rev. Lett. **99**, 257401 (2007).
[52] B. C. Larson, W. Ku, J. Z. Tischler, C.-C. Lee, O. D. Restrepo, A. G. Eguiluz, P. Zschack, and K. D. Finkelstein, Phys. Rev. Lett. **99**, 026401 (2007).
[53] J. Fink, N. Niicker, E. Pellegrin, H. Romberg, M. Alexander, and M. Knupfer, J. Electron Spectrosc. Relat. Phenom. **66**, 395 (1994).
[54] C. H. Booth and F. Bridges, Phys. Scr. **T115**, 202 (2005).
[55] C. Dallera, L. Braicovich, G. Ghiringhelli, M. A. van Veenendaal, J. B. Goedkoop, and N. B. Brookes, Phys. Rev. B **56**, 1279 (1997).
[56] J. M. Tranquada, S. M. Heald, W. Kunnmann, A. R. Moodenbaugh, S. L. Qiu, Y. Xu, and P. K. Davies, Phys. Rev. B **44**, 5176 (1991).
[57] Taiwan beamline 12XU, SPring-8, 1.2 eV resolution.
[58] R. Carboni, S. Giovannini, G. Antonioli, and F. Boscherini, Phys. Scr. **T115**, 986 (2005).